

Superior Fast-Charging Lithium-Ion Batteries Enabled by the High-Speed Solid-State Lithium Transport of an Intermetallic Cu_6Sn_5 Network

Lei-Lei Lu, Zheng-Xin Zhu, Tao Ma, Te Tian, Huan-Xin Ju,* Xiu-Xia Wang, Jin-Lan Peng, Hong-Bin Yao,* and Shu-Hong Yu*

Superior fast charging is a desirable capability of lithium-ion batteries, which can make electric vehicles a strong competition to traditional fuel vehicles. However, the slow transport of solvated lithium ions in liquid electrolytes is a limiting factor. Here, a $\text{Li}_x\text{Cu}_6\text{Sn}_5$ intermetallic network is reported to address this issue. Based on electrochemical analysis and X-ray photoelectron spectroscopy mapping, it is demonstrated that the reported intermetallic network can form a high-speed solid-state lithium transport matrix throughout the electrode, which largely reduces the lithium-ion-concentration polarization effect in the graphite anode. Employing this design, superior fast-charging graphite/lithium cobalt oxide full cells are fabricated and tested under strict electrode conditions. At the charging rate of 6 C, the fabricated full cells show a capacity of 145 mAh g^{-1} with an extraordinary capacity retention of 96.6%. In addition, the full cell also exhibits good electrochemical stability at a high charging rate of 2 C over 100 cycles (96.0% of capacity retention) in comparison to traditional graphite-anode-based cells (86.1% of capacity retention). This work presents a new strategy for fast-charging lithium-ion batteries on the basis of high-speed solid-state lithium transport in intermetallic alloy hosts.

to the development of fast-charging LIBs is the large overpotential in graphite anodes^[3,4] owing to sluggish intercalation kinetics, poor lithium transport in the liquid electrolyte, and slow solid-state diffusion in the graphite anode. The later effect would be responsible for detrimental Li plating observed on the graphite anode,^[5–7] severely affecting the cell life time and causing safety issues under fast-charging states.

Over the past several years, the overpotentials of graphite anodes have been studied in detail.^[8,9] In particular, slow transport of solvated lithium-ion in liquid electrolytes has been identified as one of the main barriers to achieve fast-charging graphite anodes with high mass loading.^[8,10–13] Under a fast-charging state, Li^+ is depleted at the bottom of the graphite anode because of the slow replenishment of Li^+ . This results in large Li^+ concentration gradients in the liquid

electrolyte and minimizes active material utilization. In particular, Li^+ depletion and concentration gradients would be further increased on increasing the thickness and decreasing the porosity of the electrodes.^[10] Notably, there is a large demand for the design of a thick electrode with a high overall energy density and greatly improved lithium-ion transportation inside the electrode.

Previous studies have been focused on electrode microstructure design with low tortuosity to reduce the lithium-ion

1. Introduction

The long charging time of lithium-ion batteries (LIBs) severely limits the global success of electric vehicles (EVs).^[1] Most currently available EVs require hours to be fully charged, which might be inconvenient for customers on a long journey that requires frequent recharging. Hence, there is a high demand for superior fast-charging LIBs, which could be charged to 80% state of charge (SOC) within 10–15 min.^[2] The main barrier

L.-L. Lu, T. Ma, S.-H. Yu
Department of Chemistry
Institute of Biomimetic Materials and Chemistry
Anhui Engineering Laboratory of Biomimetic Materials
Division of Nanomaterials and Chemistry
Hefei National Research Center for Physical Sciences at the Microscale
University of Science and Technology of China
Hefei 230026, China
E-mail: shyu@ustc.edu.cn

Z.-X. Zhu, T. Tian, H.-B. Yao
Division of Nanomaterials and Chemistry
Hefei National Research Center for Physical Sciences at the Microscale
Department of Applied Chemistry
University of Science and Technology of China
Hefei, Anhui 230026, China
E-mail: yhb@ustc.edu.cn

H.-X. Ju
PHI China Analytical Laboratory
CoreTech Integrated Limited
402 Yinfu Road, Nanjing 211111, China
E-mail: huanxin.ju@coretechint.com

X.-X. Wang, J.-L. Peng
USTC Center for Micro- and Nanoscale Research and Fabrication
Hefei 230026, China

 The ORCID identification number(s) for the author(s) of this article can be found under <https://doi.org/10.1002/adma.202202688>.

DOI: 10.1002/adma.202202688

concentration polarization effect in the liquid electrolyte.^[14,15] The design of the electrode structure can enhance Li^+ transport by reducing the migration distance. In addition, electrolyte engineering, involving variation of the solvent/salt composition, has been proposed as a technique for enhancing transport properties^[16–18] by improving the intrinsic characteristics of Li^+ transport in the liquid electrolyte.^[19,20] However, these enhanced transport properties still cannot meet the requirements for superior fast-charging LIBs mostly due to the lack of stability of the cell and increased side reactions.^[17,21]

Furthermore, electrolyte properties like high transference number^[22] and good Li ionic conductivity^[8] are vital for realizing excellent ion transport in the electrode of superior fast-charging LIBs. Inorganic solid-state lithium-ion conductors, predominantly single-ion conductors, have an ideal high transference number (t_{Li^+}) close to one. Therefore, such conductors can theoretically prevent all types of concentration polarization and have great potential for enabling fast-charging capability in LIBs.^[23,24] However, currently available inorganic solid-state electrolytes are not suitable for constructing channels for fast lithium transport within traditional graphite anodes, because of the low efficiency of solid-solid contact with electrode materials.

Herein, we developed a strategy for fast solid-state lithium transport based on a lithiated $\eta\text{-Cu}_6\text{Sn}_5$ intermetallic matrix for superior fast-charging LIBs. According to the attractive crystal structure of the matrix, we designed a solid-state Li transport network on a graphite anode using copper-tin alloy ($\text{Cu}_3\text{Sn-Cu}_6\text{Sn}_5$)-coated copper nanowires (Cu@CuSn NWs). The constructed Cu@CuSn network shows good electronic conductivity, fast solid-state lithium transport, and excellent structural stability during lithiation. Therefore, the use of our proposed graphite anode with a high-speed solid-state lithium transport channel (G-SLTC) significantly lowered the Li^+ concentration gradients and the corresponding polarization effect to levels needed for superior fast-charging LIBs (Figure 1).

2. Results and Discussion

The construction of efficient solid-state lithium transport channels in the electrodes was enabled by the unique lithiated $\eta\text{-Cu}_6\text{Sn}_5$ intermetallic crystal structure. As shown in Figure 1a, the original $\eta\text{-Cu}_6\text{Sn}_5$ has a defective NiAs-type structure,^[25] in which Cu and Sn atoms occupy the octahedral and trigonal prismatic sites of Ni and As, respectively (Figure S1a, Supporting Information). One vacant trigonal prismatic Sn site exists per Cu_6Sn_5 unit, as shown in the projection of the structure. During the lithiation process, half of the Sn atoms move in the [110] direction to form columns of Sn with neighboring Sn strings (shown by the arrows in Figure 1a). This forms a new phase with a cubic symmetry zinc blende structure (ZnS), in which the Cu and Sn atoms occupy the Zn and S sites, respectively (Figure S1b, Supporting Information). Meanwhile, the hexagonal channels with two interstitial sites are accessible for Li occupation. Through this transformation, lithiated $\text{Li}_x\text{Cu}_6\text{Sn}_5$ (full lithiation in the $\text{Li}_{13}\text{Cu}_6\text{Sn}_5$ composition, in which 17% of the Sn sites are occupied by Li) with a zinc-blende-type structure occupies a favorable 3D interstitial space for fast lithium diffusion (Figure 1b). In the fabricated G-SLTC, the 3D Cu@CuSn network through the electrode could significantly lower the Li^+ concentration gradients and the corresponding polarization effect (Figure 1c).

The Cu@CuSn NWs were synthesized via a solution-processable tin plating method on Cu nanowires (Cu NWs) as described in the Experimental Section. Briefly, Cu NWs with a diameter of 200–400 nm (Figure S2a, Supporting Information) were calcined in a H_2/Ar atmosphere and then immersed in a tin plating bath. The Sn atoms could be easily plated on the surface of Cu NWs, affording Cu@CuSn NWs via the formation of a stable complex between Cu^{2+} and the tin complex agent (Figure S2b, Supporting Information). The energy-dispersive spectrometric mapping results demonstrated that Sn

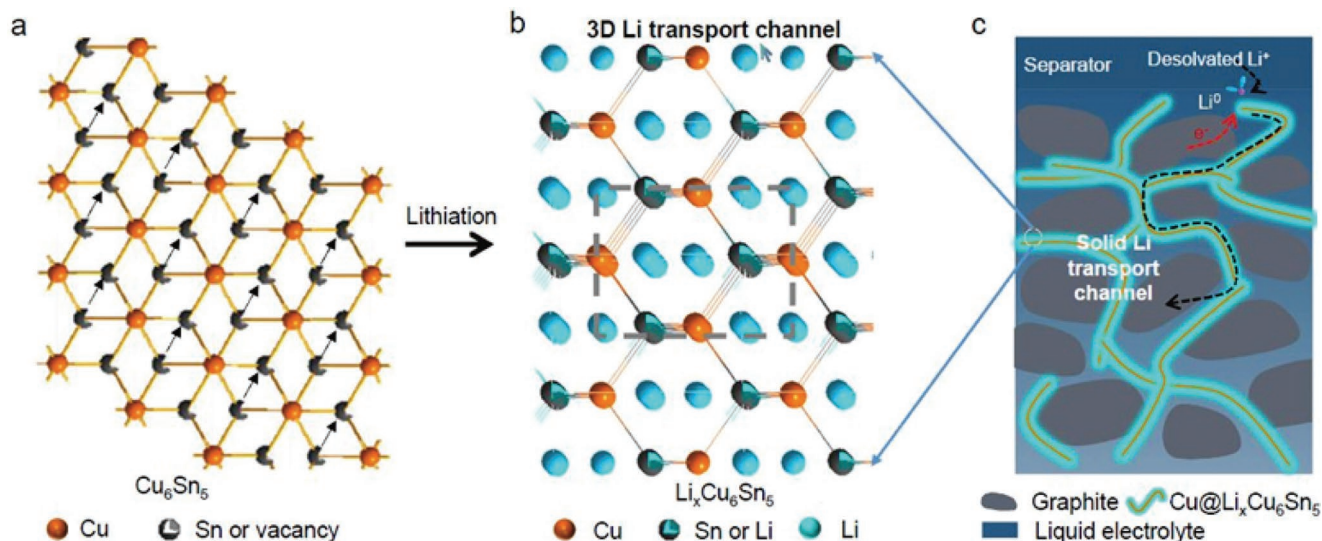


Figure 1. Schematic illustration of the construction of high-speed solid-state Li transport in the graphite anode based on the $\text{Li}_x\text{Cu}_6\text{Sn}_5$ intermetallic crystal structure. a) The crystal structure model of $\eta\text{-Cu}_6\text{Sn}_5$ ([001] projection). The arrows denote the Sn migration direction during lithium insertion. b) The crystal structure model of lithiated $\text{Li}_x\text{Cu}_6\text{Sn}_5$ ($0 < x < 13$) ([110] projection). A 3D Li transport channel is formed in the $\text{Li}_x\text{Cu}_6\text{Sn}_5$ within the zinc blende-type crystal structure. c) Solid lithium transport channel construction based on the Cu@CuSn network through the electrode to largely reduce the lithium-ion concentration gradients and the corresponding polarization in the graphite anode.

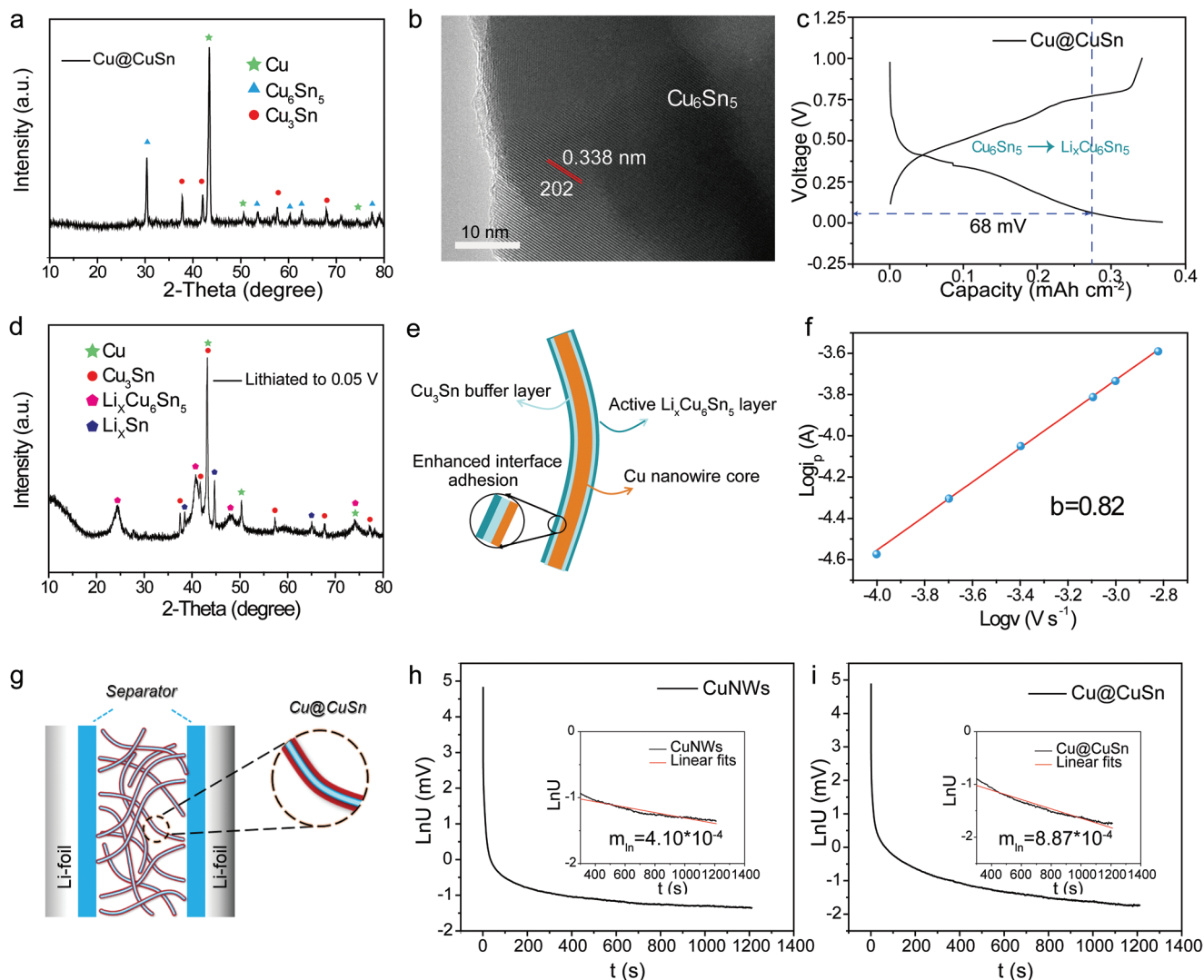


Figure 2. Characterizations of the synthesized Cu@CuSn NWs. a) PXRD patterns of the synthesized Cu@CuSn NWs. b) High-resolution TEM image of the Cu@CuSn NW showing the lattice fringes of (202) planes of intermetallic Cu_6Sn_5 . c) Typical charge–discharge curve of Cu@CuSn NW membrane. d) PXRD of Cu@CuSn NW membrane at lithiation state after 30 cycles. The charge–discharge current density is 100 mA g^{-1} . e) The schematic to show that Cu_3Sn buffer layer in the Cu@CuSn can enhance the adhesion between the Cu NW core and the $\text{Li}_x\text{Cu}_6\text{Sn}_5$ shell. f) Power-law dependence of current on the sweep rate of 0.2 V , $b = 0.82$. g) Schematic illustration of a symmetric cell geometry for testing diffusion coefficients. h, i) Plots of the relaxation phase of a steady-state polarization experiment in the cell with Cu NWs (h) and Cu@CuSn NWs (i) membrane, respectively.

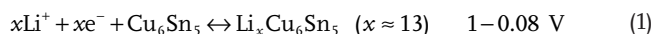
was predominantly distributed on the surface of the obtained nanowires (Figure S2c, Supporting Information), indicating the core–shell structure of the Cu@CuSn NWs. After calcination in an inert atmosphere, Cu and Sn diffused into each other's layers, forming two different Cu–Sn intermetallic compound layers, namely, Cu_3Sn and Cu_6Sn_5 , on the surface of the Cu NWs, as confirmed by the powder X-ray diffraction (PXRD) patterns (Figure 2a).

Furthermore, the effects of calcination temperature and time on the CuSn composition were investigated (Figure S3, Supporting Information). The optimal calcination conditions for the formation of lithium-inert Cu_3Sn and lithium-active Cu_6Sn_5 on the surface of the Cu NWs without other impurities were $250 \text{ }^\circ\text{C}$ and 4 h. High-resolution transmission electron microscopy (HRTEM) was employed to further investigate

composition and structure of the CuSn composite layer. As shown in Figure 2b, clear lattice fringes with a spacing of 0.338 nm , corresponding to the (202) plane of Cu_6Sn_5 at the surface of the Cu NWs, were observed. The obtained Cu@CuSn NWs exhibited superior electrical conductivity. The calculated σ of the Cu@CuSn membrane was $1.37 \times 10^6 \text{ S m}^{-1}$ similar to that of the Cu NW membrane (Table S1, Supporting Information).

We further investigated lithium intercalation in the synthesized Cu@CuSn NWs. Figure 2c shows a typical charge–discharge curve of Cu@CuSn NWs membrane, indicating reversible lithium intercalation. The long-term cycling test further indicated that Cu@CuSn possessed superior stability during lithiation/delithiation (Figure S4, Supporting Information). The PXRD pattern of Cu@CuSn in the lithiated state (charge

to 50 mV) after 30 cycles (Figure 2d) indicates that the solid lithium transport channel was still retained. This structural stability could be attributed to the chemically inert buffer layer of Cu_3Sn ^[26] during the electrochemical process, which could relieve the internal stress generated via volume expansion of the Cu_6Sn_5 layer and enhance adhesion to Cu NW core during the cycles (Figure 2e). A three-electrode test in the full cell with an over-stoichiometric negative/positive capacity ratio ($N/P = 1.1:1$) showed that the potential of the graphite anode was ≈ 68 mV in the full charge state (Figure S5, Supporting Information). This result indicates that $\text{Li}_x\text{Cu}_6\text{Sn}_5$, as the main lithiation phase, is involved in Li transport in the graphite anode during the entire charging process:^[27]



Hence, we focused on the lithiation kinetics of the transformation of Cu_6Sn_5 to $\text{Li}_x\text{Cu}_6\text{Sn}_5$. Sweep voltammetry measurements were used to determine the electrochemical properties of Cu@CuSn layer (for details, please see the Experimental Section; Figure S6a, Supporting Information). The anodic peaks at 0.2 V can be assigned to the Li intercalation forming $\text{Li}_x\text{Cu}_6\text{Sn}_5$. We assume that the current obeys the following power-law relationship:

$$i = av^b \quad (2)$$

where i is the measured current, v is the scan rate, while a and b (power-law exponent) are adjustable parameters. A high b value of 0.82 is obtained from the slope of the linear plot of $\log i$ versus $\log v$, indicating the capacitor-like nature of the lithiation kinetics (Figure 2f). The combination of capacitor-like (k_1) and diffusion-controlled (k_2) behaviors, as well as the fraction of current contributed by capacitor-like and diffusion-controlled processes, were quantified using following equation:

$$i(V) = k_1v + k_2v^{1/2} \quad (3)$$

The representative data shown in Figure S6b, Supporting Information indicate that capacitor-like charge storage (black area) constitutes the main part of the storage. The calculated capacitive contribution shows that capacitor-like capacity dominates and increases with increasing sweep speed (Figure S6c, Supporting Information). At a sweep rate of 1.5 mV s^{-1} , the capacitive contribution could reach a maximum of 80%. The capacitor-like capacity indicates that the Li intercalation reaction in $\text{Li}_x\text{Cu}_6\text{Sn}_5$ exhibits extrinsic pseudocapacitive behavior. This non-diffusion-controlled kinetic process could result in fast lithium transport at high current density during the charging process.

To further confirm how effective lithiated Cu@CuSn is in reducing the concentration polarization in the liquid electrolyte phase, the apparent diffusion coefficient (D) of the liquid electrolyte was tested as a critical parameter to determine the concentration polarization. A symmetric cell geometry (Figure 2g) was used, which is consistent with the restricted diffusion method.^[28] The pristine Cu NW membrane was used as a control sample in the symmetric cell. Before the test, both Cu@CuSn and Cu NW membranes were pre-lithiated to construct

a Li transport network. The polarization-interrupt test was performed to obtain the effective D of the electrolyte (for details, please see the Experimental Section). Figure 2h,i shows the logarithmic relaxation of the potential $\ln U(t)$ versus time after steady-state polarization (1 mA cm^{-2}) for 5 min in the cells with Cu NW and Cu@CuSn NW membranes, respectively. The insets in both figures show long-term linear fit analyses of the $\ln U(t)-t$ curves for relaxation times between 5 and 10 min. According to the theoretical model and the corresponding analytical method,^[28] the tested apparent D value of the cell with Cu@CuSn NW is twice that of the cell with Cu NW. This is because D is proportional to the slope m_{\ln} , indicating that the lithiated Cu@CuSn NW can indeed enhance Li transport in the liquid electrolyte.

To construct the solid Li transport channels in the graphite anode, Cu@CuSn NWs, a water-based binder, and graphite particles were first ball-milled to obtain a homogeneous slurry, which was then coated on a copper foil. After drying and roll pressing, the obtained graphite anode contained 2 wt% Cu@CuSn, 94 wt% active graphite, and 4 wt% binder. The areal capacity was $\approx 3 \text{ mAh cm}^{-2}$, and the porosity was below 35%. Scanning electron microscopy (SEM) images and the corresponding elementary mapping images (Figure 3a-c; Figure S7, Supporting Information) reveal a dense and uniform graphite anode morphology, in which Cu@CuSn NWs are uniformly dispersed to construct a good three-dimensionally interconnected network. The 3D X-ray image (Figure S8, Supporting Information) further confirmed that the Cu@CuSn NWs were well-dispersed inside the fabricated graphite anode, providing connected networks for electron and lithium conduction.

To demonstrate the efficiency of solid-state lithium transport through the channels in the Cu@CuSn NW network, we employed X-ray photoelectron spectroscopy (XPS) to map the spatial distribution of Li and to determine the chemical state after lithiation in the fabricated graphite anodes. The electrodes were directly lithiated via contact with a Li foil for 5 min in the presence of a liquid electrolyte. For XPS measurements, the cross section of the graphite electrode was prepared by ion milling with an argon ion beam of 10 keV, as described in the Experimental Section. An X-ray-induced secondary-electron image (SXI) was recorded using an X-ray beam size of $10 \mu\text{m}$ (Figure 3d,g). The SXI images clearly show the cross-sectional structure of the lithiated electrodes, which was used for navigation to locate the cross section for chemical state mapping. Figure 3e,h shows the overlapped mapping of the Li 1s (Li^0 and Li^+) chemical state in the lithiated G-SLTC and traditional graphite electrodes, respectively. Three zones from the top surface to the current collector were selected for mapping to obtain detailed analysis of Li distribution. As shown in Figure 3f, metallic Li^0 (54.66 eV) is the dominant chemical state (green color in Figure 3e) and is homogeneously distributed along the cross section of G-SLTC (Figure S9a, Supporting Information). In contrast, the intensity of the metallic Li^0 peak for the lithiated traditional graphite anode was much lower than that of Li^+ (56.26 eV) (Figure 3i). Moreover, Li seemed to be distributed heterogeneously, and its amount dropped rapidly along the cross section of the electrode (Figure S9b, Supporting Information). These XPS results confirmed the effectiveness of the solid-state lithium transport through the channels in the

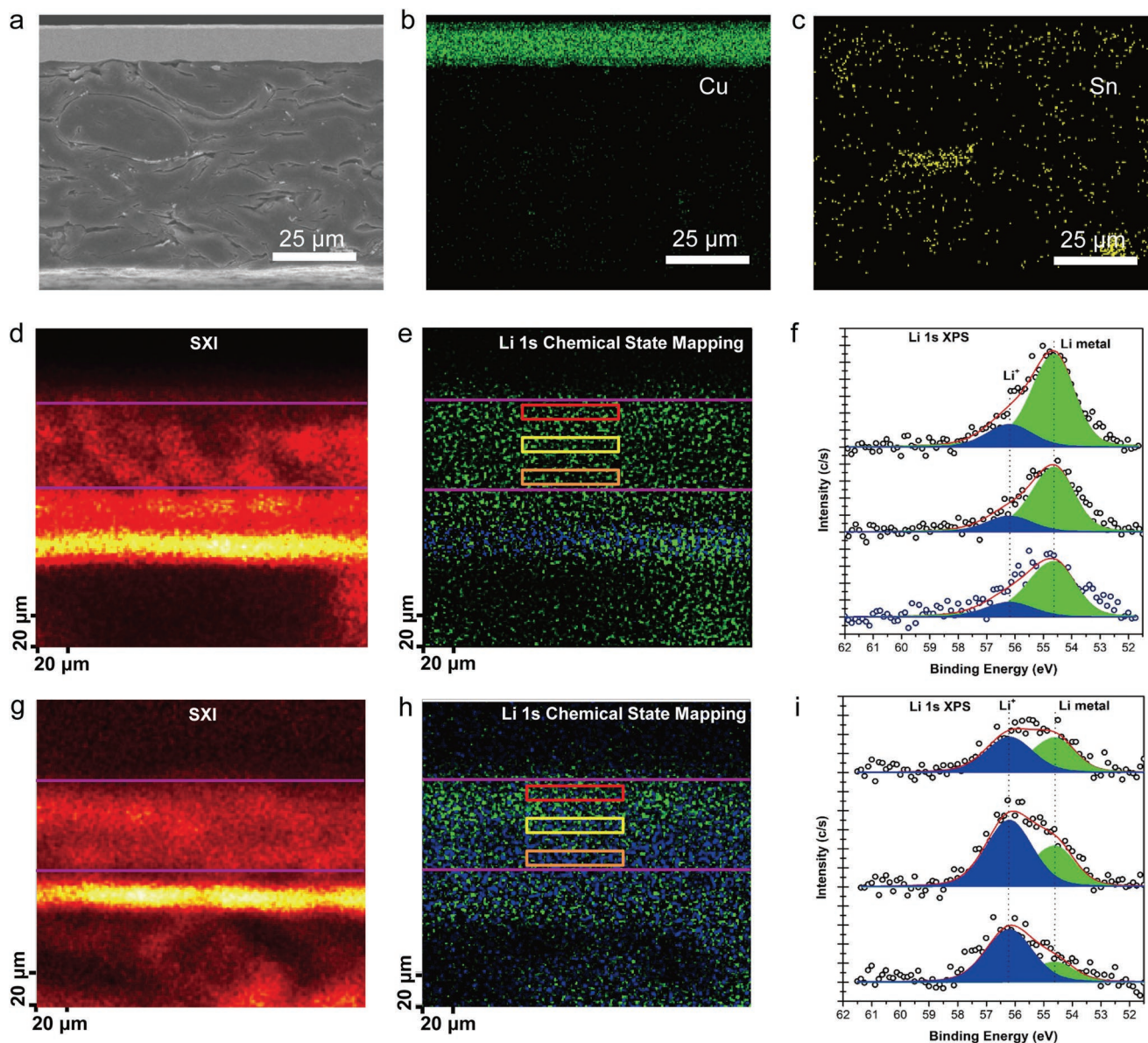


Figure 3. XPS chemical state mappings of Li 1s in the cross section of lithiated graphite anodes. a–c) The cross section SEM and the corresponding Cu and Sn elementary mapping images of G-SLTC, respectively. d–f) The Li 1s XPS mapping image of G-SLTC. The X-ray induced secondary-electron images (SXI) of the cross section (d), Li 1s overlapped chemical state mapping (e), and the corresponding XPS spectra of selected zones in Figure 3e (f). g–i) The Li 1s XPS mapping image of graphite anode. The SXI of the cross section (g), Li 1s overlapped chemical state mapping (h), and the corresponding XPS spectra of selected zones in Figure 3h (i).

constructed Cu@CuSn NW network of the graphite anode and are promising for a fast lithium transport across the graphite anode during the battery charging process.

To demonstrate the efficiency of the solid-state lithium transport across the intermetallic Cu₆Sn₅ network for improving the fast-charging performance of the graphite anode, the electrochemical performance of G-SLTC was evaluated with an areal mass loading of $\approx 10 \text{ mg cm}^{-2}$ ($\approx 3 \text{ mAh cm}^{-2}$). Impedance spectra of G-SLTC in half-cells (Figure S10, Supporting Information) show smaller semicircles in the high-frequency region, indicating that G-SLTC has a lower Li transfer resistance. As shown in Figure S11a, Supporting Information, the G-SLTC

electrode exhibits higher specific capacity and lower polarization than the traditional graphite electrode. The three-electrode test also demonstrated that G-SLTC had reduced polarization during charging (Figure S11b, Supporting Information). The differential capacity–voltage (dQ/dV – V) curve further demonstrated reduced polarization and enhanced lithium transport kinetics for the G-SLTC electrode (Figure S11c, Supporting Information). In addition, G-SLTC displayed better cycling stability at 0.2 C (1 C = 320 mA g^{-1}) than the traditional graphite electrode (Figure S11d, Supporting Information).

To demonstrate the fast-charging performance of the proposed electrode, we fabricated a full cell using the G-SLTC

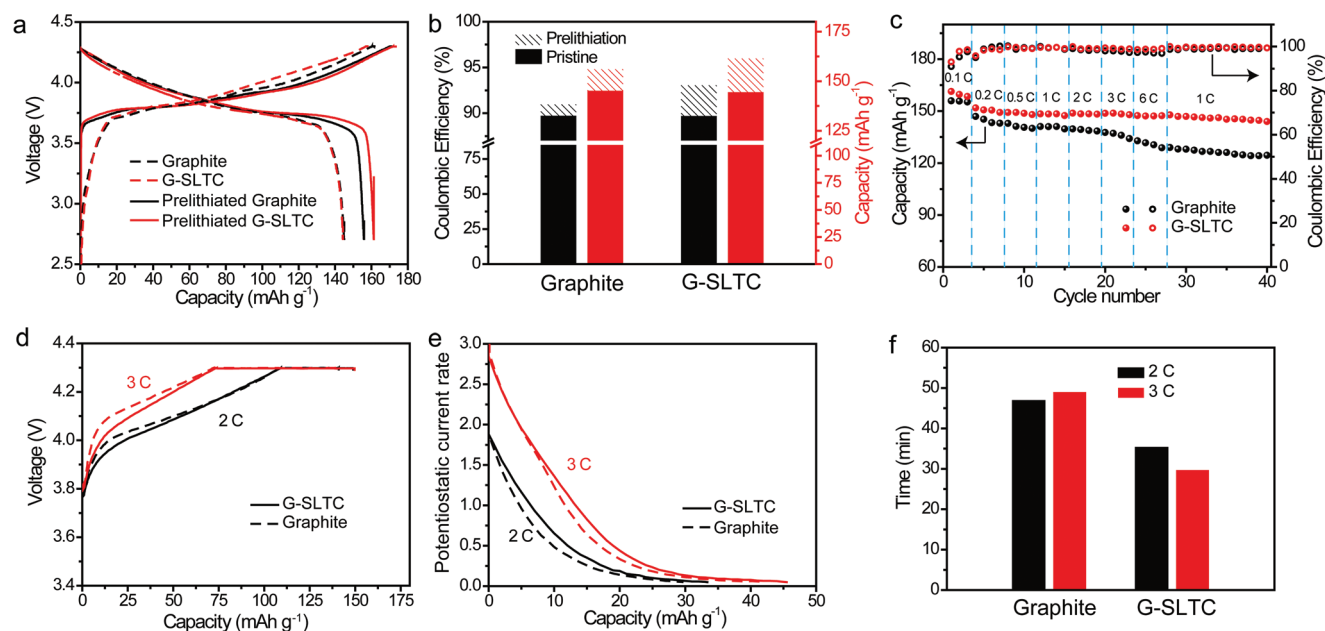


Figure 4. Fast charging performance of full cell with the G-SLTC anode and traditional graphite anode. a) Typical voltage profiles of full cells at the rate of 0.1 C. b) The improved CE and specific capacity of the cell with G-SLTC and graphite anode after pre-lithiation. c) The charging rate performance of the cells. The discharging rate is fixed at 0.5 C and the charging rate is changed from 0.2 C to 6 C. d) Typical charging voltage curves at high rate of 2 C and 3 C with constant current charging and constant voltage charging processes. e) The current rate versus capacity curve of full cells at the constant voltage process. f) Time required to charge to 140 mAh g⁻¹ at the rate of 2 C and 3 C.

as the graphite anode coupled with a LiCoO₂ (LCO) cathode and tested it in the voltage range of 2.7–4.3 V. **Figure 4a** shows that pre-lithiation could improve the capacity and first-cycle Coulombic efficiency (CE) of the cell. This is mainly due to the lower Li consumption of the LCO cathode for the solid electrolyte interphase (SEI) layer formation on the surface of the graphite anode. Especially for the G-SLTC, the observed improved CE and capacity were higher than those of the traditional graphite anode (**Figure 4b**) because the existing solid-state lithium transport channels favored pre-lithiated. **Figure 4c** shows a comparison of the specific discharge capacities of the fabricated full cells at various charging C rates. The specific discharge capacity of the cell with G-SLTC remained unchanged when the rate was increased from 0.2 C to 6 C and recovered at 1 C. Even at an extremely high charging rate of 6 C, it exhibited a capacity of 145 mAh g⁻¹ (96.6% of full capacity at 0.2 C). In contrast, the cell with the traditional graphite anode delivered a decreased capacity (116 mAh g⁻¹, i.e., 78% capacity retention) at a high charging rate of 6 C. In addition, the capacity could not be recovered at 1 C because of unwanted irreversible lithium plating on the graphite anode. The typical charging curve at high rates of 2 C and 3 C indicated that the cell with G-SLTC possessed lower polarization during a constant current process (**Figure 4d**). Even at a constant voltage, the cell containing G-SLTC exhibited lower polarization owing to the enhanced Li⁺ transport kinetics (**Figure 4e**). As a result, a higher capacity could be recharged simultaneously (**Figure S12a,b**, Supporting Information, 2 C and 3 C respectively). The corresponding time–capacity (*T–Q*) curve indicated that less time was required to reach the same SOC for the cell using G-SLTC (35 and 28 min at 2 C and 3 C, respectively) than for that using the traditional graphite anode

(47 and 49 min at 2 C and 3 C, respectively) (**Figure 4f**; **Figure S12c,d**, Supporting Information).

Further, graphite electrodes with Cu NWs (G-Cu NWs) were also fabricated to demonstrate the effect of Cu@CuSn. As shown in **Figure S13a**, Supporting Information, the *T–Q* curves of the full cell at a high charging rate of 2 C indicated that the G-Cu NWs could be charged a lower capacity than the G-SLTC, which is even lower than that of the graphite anode. The rate performance of the full cells (**Figure S13b**, Supporting Information) shows that the full cells working with G-Cu NWs exhibit lower galvanostatic charge capacities than the full cells working with G-SLTC at different charging current rates, especially at high current rates. These results demonstrated that the enhanced fast-charging performance was attributed to the high-speed transport of the solid Li and not an electron conductivity effect.

The cycling stability of LIBs at a high charging rate is a primary parameter for the fast-charging performance evaluation of the cell life span. Cycling stability tests showed that the cell with G-SLTC has good capacity retention over 100 cycles (96.0% at 2 C, **Figure 5a**; 80.7% at 3 C, **Figure S14**, Supporting Information), whereas the cell with the traditional graphite anode exhibited drastic capacity fading after 100 cycles (86.1% at 2 C and 64.3% at 3 C). The voltage profiles of the full cells at a charging rate of 2 C after multiple cycles were extracted to investigate its stability at high charging rates. Typical voltage profiles after 50 (**Figure S15a**, Supporting Information) and 100 cycles (**Figure S15b**, Supporting Information) at a rate of 2 C indicated lower polarization and less charging time for the cell with G-SLTC than for the cell with the traditional graphite anode. The time needed to charge to 80% SOC for multiple cycles at 2 C indicated that the cell with G-SLTC could retain a constant

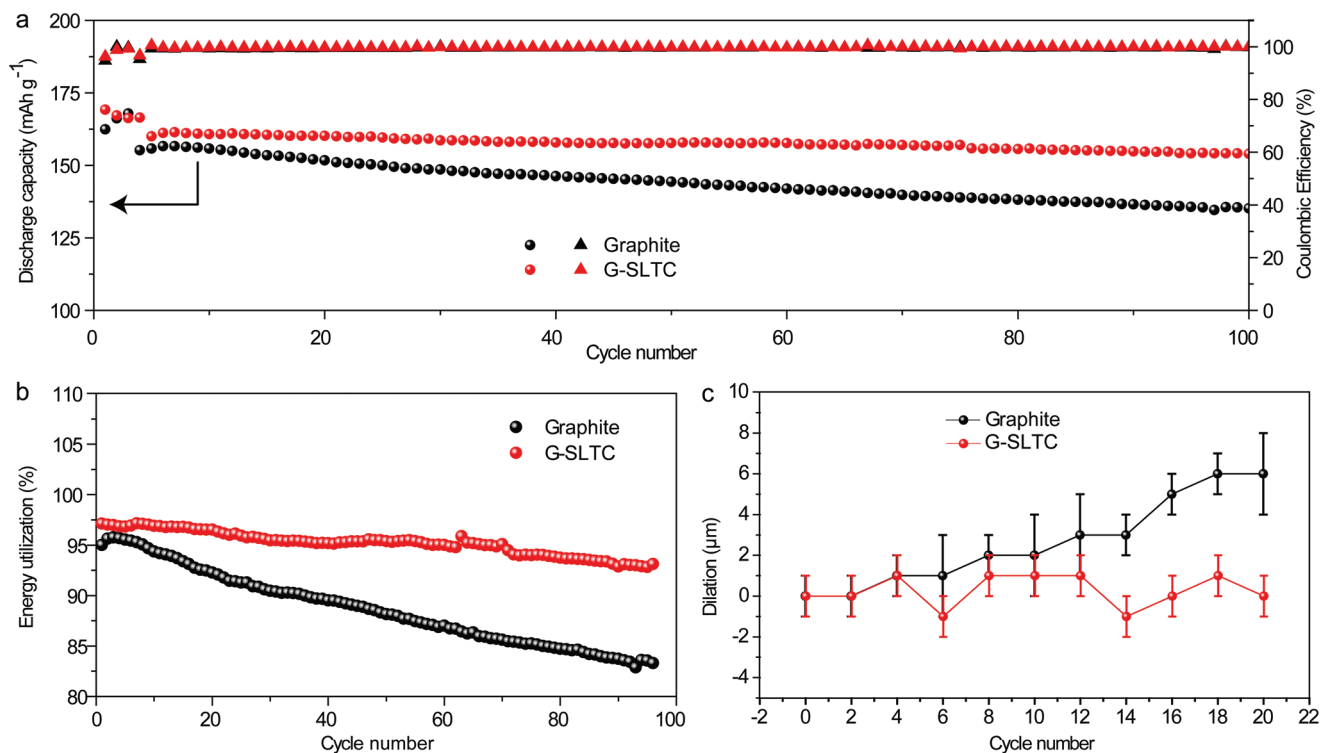


Figure 5. Electrochemical stability of full cell at high charging rate. a) Long-term cycling performance of full cell at a high charging rate of 2 C. The discharging rate is fixed at 0.5 C. b) The battery energy utilization of full cells in the long-term cycles. The battery energy utilization is defined as the ratio of the charging energy to the discharging energy. c) Irreversible increase in the thickness of the electrode at delithiated state for 20 cycles.

charging time of 30 min to reach SOC. In contrast, the charging time of the cell with the traditional graphite anode increased rapidly with increasing number of cycles (Figure S15c, Supporting Information).

Battery energy utilization, defined as the ratio of the charging energy to the discharging energy, was also investigated to evaluate the electrochemical stability of the fabricated cell. As shown in Figure 5b, the cell with G-SLTC exhibited a superior energy retention of 95% after 100 cycles. In contrast, the cell with the traditional graphite anode presented a significant drop of the energy utilization, where only 82% of the energy was retained after 100 cycles. The drop in energy utilization could be attributed to the increased energy consumption due to the large concentration polarization and/or the sudden Li deposition.^[29] To verify whether Li deposition occurred, the irreversible change in the electrode thickness was analyzed via dilatometry in the pouch cell (Figure 5c). The cell with the traditional graphite anode exhibited a rapid and continuous increase in dilatation due to metallic lithium deposition at a high charging rate of 2 C, resulting in drastic capacity drop (Figure S16, Supporting Information). In contrast, there was little dilatation and good capacity retention after 50 cycles in the cell with G-SLTC (Figure 5c; Figure S16, Supporting Information, respectively).

3. Conclusion

In summary, we propose a new strategy for using Cu₆Sn₅ intermetallic compound as a novel Li⁺ intercalation material

to greatly reduce the already existent large liquid-phase polarization during the charging process. This, in-turn, results in a much enhanced fast-charging performance with excellent cycle life in practical graphite/LCO full cells under rigorous conditions, including a high active material loading (>3 mAh cm⁻²) and low porosity (<35%). In particular, the full cell with G-SLTC displayed stable cycling at a high charging rate of 2 C with a low capacity fading rate of 0.04% per cycle over 100 cycles, without any trace of lithium plating. The preparation of G-SLTC is feasible and compatible with the commercial LIB preparation process. Above all, this new strategy overcomes the major trade-off between the fast-charging capability and high energy density of LIBs and will open new avenues in the development of excellent fast-charging and high-energy-density LIBs.

4. Experimental Section

Synthesis of the Cu@Cu₃Sn-Cu₆Sn₅ Nanowires: First, the Cu NWs were synthesized according to the previous literature.^[1] Briefly, Cu NWs were synthesized by reducing the Cu²⁺ by hydrazine in the mixture solution of NaOH (350 mL, 15 M), EDA (5 mL) at 80 °C. After the reaction, the yield Cu NWs were washed by deionized water and ethanol for several times and dried at 80 °C in a vacuum oven for 12 h. The desiccated Cu NWs were then annealed under the H₂/Ar (5%/95%) flow at 450 °C for 4 h for the surface reduction. To obtain the Cu@Cu₃Sn, the reduced Cu NWs was dispersed into the industrial tin plating solution (BEICHEN Ltd.) for 3 min. After washed by deionized water and ethanol for several times and dried at 80 °C in a vacuum oven for 8 h, the obtained Cu@Cu₃Sn nanowires were annealed under the H₂/Ar (5%/95%) at 250 °C to form the final Cu@Cu₃Sn-Cu₆Sn₅ nanowires.

Electrode Preparation: The CuNWs membrane was formed via the self-evaporation of ethanol solvents of the CuNWs solution and then annealed under the H₂/Ar (5%/95%) flow. The Cu@CuSn membrane electrode was prepared by the infusion of CuNWs membrane into the industrial tin plating solution. For the preparation of G@SLTC, 4.23 g synthetic graphite (BTR Co., Ltd.), 90 mg Cu@CuSn NWs, and 180 mg aqueous binder in a mass ratio of 94:2:4 were mixed in 5 mL deionized water and 0.2 mL ethanol. Then, the suspension was poured into 50 mL zirconia ball mill tank and mixed well by high-energy planet ball-milling at 350 rpm for 4 h. The obtained homogeneous slurry was coated onto a Cu foil by a 250 μm doctor blade and dried at 90 °C for 12 h. Then the electrode was calendered (MSK-HRP-01, MTI) to form a dense anode with density greater than 1.5 g cm⁻³. The obtained G-SLTC electrode had a graphite mass loading of ≈10 mg cm⁻². As a comparison, the traditional graphite electrode was prepared by using same mass of carbon black to replace Cu@CuSn NWs. To fabricate the lithium cobalt oxides (LCO, BTR Co., Ltd.) cathode, the homogeneous slurry containing LCO, carbon black, and polyvinylidene fluoride (PVDF) in a mass ratio of 90:5:5 were mixed in 6 mL 1-methylpyrrolidone (NMP) and coated onto aluminum foils by a 500 μm doctor blade and dried in a vacuum oven at 100 °C for 12 h. The LCO electrode with a mass loading of 22–24 mg cm⁻² was calendered. In the full cell, capacity ratio of negative to positive electrode (N/P ratio) was controlled into 1.05–1.1.

Polarization-Interrupt Experiment: The symmetric cell was assembled in the stainless-steel 2032-coin cells. The pre-lithiation of CuNWs and Cu@CuSn membranes was conducted by directly contacting with Li foil for 5 min. Galvanostatic pulse polarization experiments were conducted using the two electrode symmetrical lithium cell shown in Figure 2g. Several cycles were performed on the cells to form a stable SEI on the lithium electrodes. Subsequently, a polarization (U_0) induced by concentration gradient was set up by applying a constant current (1 mAcm⁻²) for 5 min in the cell. Then, a concentration gradient was relaxed by interrupting the current until the cell potential approached zero (≈5–10 mV). Then the current direction was reversed followed by interruption. The relaxation of the concentration gradient was observed in terms of a cell-potential decay with the time (Figure 3h,i). The long-term relaxation behavior was investigated for the determination of the diffusion coefficient. The relaxation of the concentration profile could be observed via the relaxation of the cell potential $U(t)$. By the mathematical derivation, the effective diffusion coefficient could be calculated from the linear simulated slope m_{in} in the zone of long-term relaxation:

$$D_{\text{eff}}(C_0) = \frac{l^2}{\pi^2} m_{in} \quad (4)$$

Electrochemical Testing: All electrochemical tests were conducted in the stainless-steel 2032 coin cells. The electrolyte contains 1.0 M LiPF₆ dissolved in 1.1:1 v/v/v ethylene carbonate/ethyl methyl carbonate/dimethyl carbonate (Duoduo Reagents, battery grade) with 2% vinylene carbonate as additive. Celgard 2400 was used as the separators. All cells were assembled in an argon-filled glove box (H₂O < 0.5 ppm, O₂ < 0.5 ppm). The tests were performed at a room temperature around 25 °C.

In a half-cell, the graphite electrode was coupled with Li metal foil (TIANQI LITHIUM, 99.95%) as the counter electrode. The cyclic voltammetry (CV) rate test of Cu@CuSn film electrode was conducted with a sweep rate from 0.1 to 1.5 mV s⁻¹ in a voltage range of 0–1.0 V. All the cells were activated to form stable SEI in the first cycle. In the activation process, the cells were discharged to 5 mV at a rate of 0.05 C followed 5 min static duration and were discharged to 5 mV repeatedly at a low current density of 50 μA. The cells were then charged to 1 V at 0.1 C.

The full cells were assembled with LCO as the cathodes. The voltage range in the tests was 2.7–4.3 V. The CC-CV charge mode was taken to investigate the charging rate performance to ensure the cells reproducible condition at the end of each cycle. The full cells were charged at a various current to a cut-off potential of 4.3 V followed a subsequent potentiostatic stabilization at 4.3 V until the specific current

dropped to below 0.02 C. The current densities in the constant current process progressively increased from 0.2 C to 6 C. The ensuing discharge was performed at 0.5 C. Four consecutive cycles were performed for each C-rate.

A three-electrode test was conducted in a home-made coin cell with lithiated lithium titanate (Li_{4+x}Ti₅O₁₂) as reference electrode. To fabricate the reference electrode, the Li₄Ti₅O₁₂ slurry (Li₄Ti₅O₁₂:AB:PVDF = 8:1:1 in NMP) was first casted on a tip-flattened copper wire. The Li₄Ti₅O₁₂ electrode was lithiated and delithiated at 0.1 C for 5 cycles and kept static subsequently at lithiated state to obtain a stable open-circuit voltage as reference electrode the potential (1.565 V). The reference electrode was embedded in the full cell with an over-stoichiometric negative/positive ratio (N/P = 1.1:1). The full cells were charged and discharged in the voltage 2.7–4.3 at 0.1 C to obtain the corresponding charge–discharge curve of anode and cathode.

Characterizations: SEM (JEOL-6700F) was employed to carry out the morphologies and elemental mapping of Cu NWs and Cu@CuSn compound. XRD patterns were collected on a Philips X'Pert PRO SUPER X-ray diffractometer equipped with graphite monochromatized Cu Kα radiation. Ion Beam Sampling (IBS, EMTIC 3X, LEICA Company) was employed to fabricate a flat cross-sectional surface of samples using argon (Ar) ion beam at 10 keV. XPS microanalysis was conducted on PHI 5000 VersaProbe III with a micro focused scanning Al Kα X-ray source and cross section samples were transferred from the glove-box to the intro-chamber by a transfer vessel without exposing to air. The SEM images of the cross-sectional surfaces were taken in a SE mode at 5 keV (SU8220, HITACHI). The laboratory-based X-ray tomography technique (Xradia Versa XRM-500 system, Carl Zeiss X-ray Microscopy Inc.) was adopted to collect the reconstructed 3D tomography data. The irreversible volume expansion of the electrode was measured at delithiated state as the thickness difference in different cycles. Thickness change was estimated by dilatometer.

Supporting Information

Supporting Information is available from the Wiley Online Library or from the author.

Acknowledgements

L.-L.L. and Z.-X.Z. contributed equally to this work. The authors acknowledge the funding support from the National Natural Science Foundation of China (Grants: U1932213, 51732011, 51571184, 21501165, 21875236, 21573211, and 21905264), the National Basic Research Program of China (Grant: 2021YFA0715700), the Anhui Provincial Natural Science Foundation (Grant: 2008085QB51), the Joint Funds from Hefei National Synchrotron Radiation Laboratory (Grant KY2060000111), the National Postdoctoral Program for Innovative Talents (Grant: BX20180283), and China Postdoctoral Science Foundation (Grants: 2019M652206, 2019M663086). This work was partially carried out at the USTC Center for Micro- and Nanoscale Research and Fabrication. The authors thank Jin-Lan Peng for their help with electrode cross section preparation and SEM observation.

Conflict of Interest

The authors declare no conflict of interest.

Data Availability Statement

The data that support the findings of this study are available from the corresponding author upon reasonable request.

Keywords

fast-charging batteries, graphite/lithium cobalt oxide full cell, intermetallic Cu₆Sn₅ networks, lithium-ion batteries, solid-state Li transport

Received: March 23, 2022

Revised: June 13, 2022

Published online: July 7, 2022

-
- [1] Y. Liu, Y. Zhu, Y. Cui, *Nat. Energy* **2019**, *4*, 540.
- [2] P. A. Nelson, D. C. Robertson, T. Stephens, R. Vijayagopal, R. B. Carlson, F. Dias, E. J. Dufek, C. J. Michelbacher, M. Mohanpurkar, D. Scofield, M. Shirk, T. Tanim, M. Keyser, C. Kreuzer, O. Li, A. Markel, A. Meintz, A. Pesaran, S. Santhanagopalan, K. Smith, E. Wood, J. Zhang, *Technical Report: Enabling Fast Charging: A Technology Gap Assessment*, US Department of Energy, Office of Energy Efficiency and Renewable Energy, October **2017**, <https://doi.org/10.2172/1416167>.
- [3] S. Ahmed, I. Bloom, A. N. Jansen, T. Tanim, E. J. Dufek, A. Pesaran, A. Burnham, R. B. Carlson, F. Dias, K. Hardy, *J. Power Sources* **2017**, *367*, 250.
- [4] J. B. Goodenough, Y. Kim, *Chem. Mater.* **2010**, *22*, 587.
- [5] Z. Li, J. Huang, B. Y. Liaw, V. Metzler, J. Zhang, *J. Power Sources* **2014**, *254*, 168.
- [6] T. Waldmann, B.-I. Hogg, M. Wohlfahrt-Mehrens, *J. Power Sources* **2018**, *384*, 107.
- [7] X.-G. Yang, G. Zhang, S. Ge, C.-Y. Wang, *Proc. Natl. Acad. Sci. USA* **2018**, *115*, 7266.
- [8] A. M. Colclasure, A. R. Dunlop, S. E. Trask, B. J. Polzin, A. N. Jansen, K. Smith, *J. Electrochem. Soc.* **2019**, *166*, A1412.
- [9] A. M. Colclasure, T. R. Tanim, A. N. Jansen, S. E. Trask, A. R. Dunlop, B. J. Polzin, I. Bloom, D. Robertson, L. Flores, M. Evans, E. J. Dufek, K. Smith, *Electrochim. Acta* **2020**, *337*, 135854.
- [10] K. G. Gallagher, S. E. Trask, C. Bauer, T. Woehrle, S. F. Lux, M. Tschech, P. Lamp, B. J. Polzin, S. Ha, B. Long, Q. Wu, W. Lu, D. W. Dees, A. N. Jansen, *J. Electrochem. Soc.* **2015**, *163*, A138.
- [11] C. Mao, R. E. Ruther, J. Li, Z. Du, I. Belharouak, *Electrochem. Commun.* **2018**, *97*, 37.
- [12] A. Nyman, T. G. Zavalis, R. Elger, M. r. Behm, G. r. Lindbergh, *J. Electrochem. Soc.* **2010**, *157*, A1236.
- [13] M. F. Hasan, C.-F. Chen, C. E. Shaffer, P. P. Mukherjee, *J. Electrochem. Soc.* **2015**, *162*, A1382.
- [14] J. Billaud, F. Bouville, T. Magrini, C. Villevieille, A. R. Studart, *Nat. Energy* **2016**, *1*, 16097.
- [15] I. V. Thorat, D. E. Stephenson, N. A. Zacharias, K. Zaghib, J. N. Harb, D. R. Wheeler, *J. Power Sources* **2009**, *188*, 592.
- [16] E. R. Logan, E. M. Tonita, K. L. Gering, J. Li, X. Ma, L. Y. Beaulieu, J. R. Dahn, *J. Electrochem. Soc.* **2018**, *165*, A21.
- [17] D. S. Hall, A. Eldesoky, E. R. Logan, E. M. Tonita, X. Ma, J. R. Dahn, *J. Electrochem. Soc.* **2018**, *165*, A2365.
- [18] X. Ma, R. S. Arumugam, L. Ma, E. Logan, E. Tonita, J. Xia, R. Petibon, S. Kohn, J. R. Dahn, *J. Electrochem. Soc.* **2017**, *164*, A3556.
- [19] L. O. Valo/en, J. N. Reimers, *J. Electrochem. Soc.* **2005**, *152*, A882.
- [20] M. Doyle, T. F. Fuller, J. Newman, *Electrochim. Acta* **1994**, *39*, 2073.
- [21] X. Ma, J. Li, S. L. Glazier, L. Ma, K. L. Gering, J. R. Dahn, *Electrochim. Acta* **2018**, *270*, 215.
- [22] K. M. Diederichsen, E. J. McShane, B. D. McCloskey, *ACS Energy Lett.* **2017**, *2*, 2563.
- [23] T. Famprikis, P. Canepa, J. A. Dawson, M. S. Islam, C. Masquelier, *Nat. Mater.* **2019**, *18*, 1278.
- [24] Y. Kato, S. Shiotani, K. Morita, K. Suzuki, M. Hirayama, R. Kanno, *J. Phys. Chem. Lett.* **2018**, *9*, 607.
- [25] K. D. Kepler, J. T. Vaughey, J. T. , M. M. Thackeray, *Electrochem. Solid-State Lett.* **1999**, *2*, 307.
- [26] X. F. Tan, S. D. McDonald, Q. Gu, Y. Hu, L. Wang, S. Matsumura, T. Nishimura, K. Nogita, *J. Power Sources* **2019**, *415*, 50.
- [27] J.-j. Zhang, P. He, Y.-y. Xia, *J. Electroanal. Chem.* **2008**, *624*, 161.
- [28] A. Ehrl, J. Landesfeind, W. A. Wall, H. A. Gasteiger, *J. Electrochem. Soc.* **2017**, *164*, A826.
- [29] Q. Liu, C. Du, B. Shen, P. Zuo, X. Cheng, Y. Ma, G. Yin, Y. Gao, *RSC Adv.* **2016**, *6*, 88683.